Chapter 7

Applications of Fiber-Optic Interferometry Technology in Sensor Fields

Lutang Wang and Nian Fang

Additional information is available at the end of the chapter

http://dx.doi.org/10.5772/66276

Abstract

Optical interferometry as a precision metrology has been widely employed in many aspects for accurate measurements of various physical quantities. As an important branch of measurement technology, now the fiber-optic interferometry technology, based on fiber-optic and laser technologies, has been developed and widely applied in sensor fields for detections of various unknown or uncontrolled physical parameters. In this chapter, basic concepts of fiber-optic interferometry are presented and clarified. Also, three novel fiber-optic sensors, based on the optical interferometry technology and mainly used in the power industry for equipment failure monitoring, are demonstrated.

Keywords: optical interferometry, laser, fiber-optic sensor, interference fringe, fiber Bragg grating-based interferometer

1. Introduction

Optical interferometry, as a precision metrology widely used in the optical system for extremely accurate measurements of a variety of physical quantities in laboratories as well as in industry fields [1], has been developed for over a hundred years. The optical interferometry technology is based on the interference of light beams, two beams or multiple beams, launched from same light source, laser source, or other monochromatic source, propagating through space or dielectric mediums such as glass waveguides with different optical paths, and arriving simultaneously at a point in space or on the surface of an object. As a result, the light intensity will vary periodically with the optical path difference, that is the optical phase difference, between the beams [2]. This is the well-known phenomenon of light

interference. The periodic change in the intensity of interference light is usually referred to as the interference pattern or the interference fringe [2]. A very small change in the optical path difference in the wavelength scale of light source can induce an obvious and measurable change in the intensity of the interference light. Therefore, by measuring the changes of interference light intensity, one can get the information about the changes of optical paths in an optical measurement system. Based on this mechanism, the optical interferometer is built as an instrument and is widely used for accurate measurements of many physical quantities, such as the distance, displacement, and velocity as well as for tests of optical systems.

With quick developments of laser and fiber optic technologies, the optical interferometry technology also had great progress and evolved from the classical bulk optics to the fiber optics [3]. Based on fiber-optic technologies, applications of the optical interferometers have been expanded to such areas as underwater acoustic detections, voltage and current measurements inside electric power systems [3–7], and biomedical pressure monitoring in living bodies [8]. As one of the most important applications, the optical interferometer is used as the optical interferometer sensor for detections of unknown and uncontrolled physical parameters [3]. The fiber-optic-based interferometer sensor uses optical fibers as light carriers and obtains the detection information from fiber-connected transducers or directly from fibers themselves [3, 8]. Compared with the classical, bulk-optic interferometer sensors, the fiber-optic interferometer sensors can achieve remote sensing and have a number of attractive features, such as excellent sensitivity and large dynamic range, small size with rugged packages, potential for low cost, and high reliability. In general, optical fibers and fiber-optic transducers/sensors are made with totally dielectric materials that are chemically inert and completely immune to electromagnetic interference (EMI), and can also withstand relatively high temperatures [4, 5, 8]. These unique properties make them very favorable to be used in harsh environments [9, 10], such as inside an electric power system in which the strong EMIs often make conventional electronic sensors work unstable and result in the increase of the fault rate.

The main aim of this chapter is to give a brief introduction of optical interferometers based on fiber-optic technology and their practical applications in the electric power industry for monitoring of the power system's running states, as well as for measuring of some crucial physical parameters. In Section 2, we will roughly classify the most commonly used fiber interferometers, according to their architectures, operation principles, and application areas. As a key fiber-optic component, the fiber Bragg grating plays a very important role in the constitution of an in-line fiber-optic interferometer [9, 11, 12], so the principles of the fiber Bragg grating as well as twin-grating-based fiber interferometer also will be introduced briefly. In Section 3, three prototypes of fiber interferometer sensors, developed in our laboratory recently, and intentionally used in the electric power industry for partial discharge (PD) sensing and the measurements of power-frequency electric field strength, are presented. Some preliminary experimental results for demonstrating the performances of these sensors also are presented. In the final section, a conclusion for summarizing our work is given to close this chapter.

http://dx.doi.org/10.5772/66276

2. General principles

As an analog of bulk-optic interferometer, the fiber-optic interferometer follows many elementary physical principles and concepts similarly adopted in the bulk-optic interferometer. Although the optical fibers provide many unique features which make the performances of the interferometer system be improved greatly, the optical fiber properties such as the birefringence, dispersion, and temperature dependence as well as nonlinear effects still influence the ultimate performances of a fiber interferometer system [4, 13]. Therefore, when we design a novel fiber interferometer system, discuss its performances, and explore new applications, a variety of fiber properties have to be taken into account. The fiber interferometers now are most commonly employed for industrial measurements and sensor applications [5, 6, 12, 14]. According to their architectures, these fiber interferometers may be simply classified into four dominant types, as schematically illustrated in **Figure 1**. They are the fiber Mach-Zehnder, Michelson, Sagnac, and Fabry-Perot interferometers.

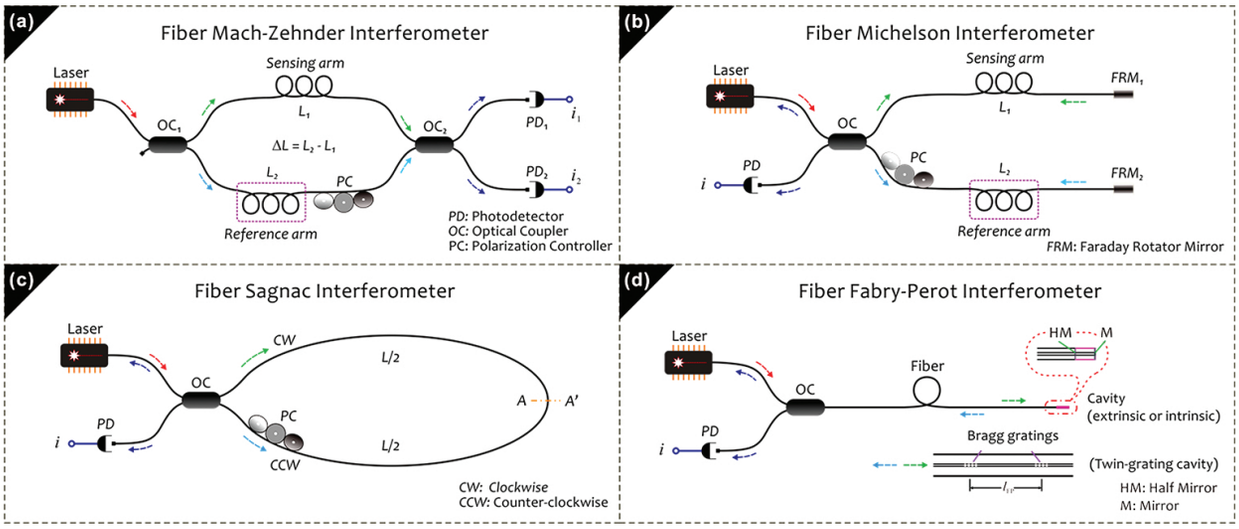

Figure 1. Configurations of main fiber interferometers. (a)–(d) are fiber Mach-Zehnder, Michelson, Sagnac, and Fabry-Perot interferometers, respectively.

2.1. Fiber Mach-Zehnder interferometer

A common two-beam fiber-optic interferometer is the fiber Mach-Zehnder interferometer [2, 4]. As shown in **Figure 1(a)**, the optical paths consist of two fiber arms, one to be assigned as *signal* arm with a length l_s and the other one as *reference* arm with a length l_r. The light beam from a light source is amplitude-divided by a fiber coupler OC_1 into two beams propagating respectively in *signal* and *reference* arms. In general, the *signal* arm is exposed to the external environment to sense disturbances, while the *reference* arm is kept in a relatively constant environment. The phase of the *signal* beam is modified by the external disturbances as a physical measurand when the beam passes through the *signal* arm. It produces a phase difference between two beams, *signal* beam and *reference* beam, which recombine at a second

fiber coupler OC_2. Two groups of beams output from the two ports of OC_2 are then detected by two photodetectors, PD_1 and PD_2, and converted into a pair of fringe signals in antiphase. If total optical losses in the interferometer are negligible, the two fringe signal intensities, P_1 and P_2, can be expressed as [4]:

$$P_1 \propto I_1 + I_2 + \xi \cdot \gamma \cdot 2\sqrt{I_1 I_2}\cos(\Delta\varphi) \tag{1}$$

$$P_2 \propto I_1 + I_2 - \xi \cdot \gamma \cdot 2\sqrt{I_1 I_2}\cos(\Delta\varphi) \tag{2}$$

where $\Delta\varphi = \varphi_s - \varphi_r$ is the phase difference, $\varphi_s = 2\pi n l_s/\lambda$ and $\varphi_r = 2\pi n l_r/\lambda$ are the phases of the *signal* beam and *reference* beam, respectively, and n is the refractive index of the fiber core; I_1 and I_2 are the intensities of *signal* beam and *reference* beam arose at output ports of OC_2, respectively; ξ is a ratio, $0 \le \xi \le 1$, reflecting the matching degree of two beams in their polarization states, which is adjustable by an in-line polarization controller PC, as shown in **Figure 1(a)**; γ is defined as the fringe visibility [2], $0 \le \gamma \le 1$, in relation to I_1 and I_2

$$\gamma = 2\sqrt{I_1 I_2}\,/\,(I_1 + I_2) \tag{3}$$

Also, γ is a function of the product of the spectral line width $\Delta\nu$ of the light source and the optical path difference $\Delta l = n(l_s - l_r)$, given by

$$\gamma(\Delta\nu \cdot \Delta l) \le 1 \tag{4}$$

For $\Delta\nu \cdot \Delta l = 0$, $\gamma \equiv 1$. In general, for getting a strong contrast on the interference fringe, $\gamma(\Delta\nu \cdot \Delta l) \sim 1$ is required. For a known $\Delta\nu$, when $\gamma = e^{-1}$, Δl corresponds with the coherence length l_c of the light source [4], having $l_c = \Delta l$.

2.2. Fiber Michelson interferometer

The fiber Michelson interferometer also is a two-beam optical interferometer [4], so its output can be similarly described by Eq. (1) or (2). In the system structure, the fiber Michelson interferometer is very similar to the fiber Mach-Zehnder interferometer. As shown in **Figure 1(b)**, the *signal* and *reference* arms are terminated by two mirrors or Faraday rotator mirrors, so that the *signal* beam and *reference* beam, both are reflected by corresponding mirrors back to the coupler OC where they are recombined to generate the interference signal. It is noted that the phase difference $\Delta\varphi = 2(\varphi_s - \varphi_r)$ in the fiber Michelson interferometer is double of that in the fiber Mach-Zehnder interferometer, which, therefore, will effectively double the sensitivity of interferometer.

2.3. Fiber Sagnac interferometer

The fiber Sagnac interferometer is a special and important two-beam, common-path interferometer system [2, 4], in which, as shown in **Figure 1(c)**, two beams from the coupler OC traverse the same fiber loop in opposite directions, usually referred to as the clockwise (CW) and the counter-clockwise (CCW) directions, respectively. The interference fringe is generated when CW and CCW beams, after traveling the whole fiber loop, recombine at OC. Since the optical paths traversed by two beams are very nearly equal, at first sight, the optical phase difference between two beams would always be zero, which represents a static state. However, when the external measurand, such as the acoustic wave, disturbs the fiber close to one end of the loop, an instant phase shift arises. This property makes the Sagnac interferometer be particularly well suited for sensing rapidly varying environmental perturbations. In the early years, the fiber Sagnac interferometer had been developed principally for the purpose of measuring the angle velocity [15], as a fiber gyroscope [4, 16]. Now it has become an important sensor used in the electric power industry for sensing of various physical parameters, such as currents, voltages, electric and magnetic fields, and vibrations as well as acoustic emissions from the partial discharges occurring inside the high-voltage power equipment [17–19].

Similarly, as a two-beam interferometer, the two outputs of fiber Sagnac interferometer also can be expressed by Eqs. (1) and (2). It should be noted that since the optical path difference in the Sagnac interferometer is almost zero, any type of the light source with low or high coherence can be employed.

2.4. Fiber Fabry-Perot interferometer

As shown in **Figure 1(d)**, the fiber Fabry-Perot interferometer actually is a multiple-beam interferometer system and consists of an interferometric cavity formed by two parallel reflectors (half mirrors) with reflectance R on either side of an optically transparent medium with a length l_{FP} [2, 4]. The available cavity structures, usually determined by the applications or design requirements, may be the extrinsic or intrinsic type [12, 20–24]. As illustrated in **Figure 1(d)**, in the extrinsic-type structure, the two reflectors are separated by an air gap or by some solid or liquid material other than the fiber, so that the measurand affects only the optical length of cavity other than the fiber. Here the fiber is used only as a light channel to transport the light beams to and from the interferometer. In contrast, in the intrinsic version, the cavity usually is constructed within the fiber as an integral part of a continuous fiber with two internal reflectors formed by flat-cut fiber ends or by fiber Bragg gratings [12, 22]. Compared with the fiber Mach-Zehnder and Michelson interferometers, the fiber Fabry-Perot interferometer is quite compact in size and therefore available as a point sensor for some applications, such as the smart structure sensing applications [23, 24].

The interference fringe, as a result of multiple reflections of the beam in the cavity, is much narrower than the normal two-beam fringes and becomes much sharper with the increase of the reflectance R. The finesse F, a parameter frequently used to characterize the overall performance of a Fabry-Perot interferometer, in relation to the sharpness of fringe, is defined as the ratio of the separation of adjacent fringes to their width FWHM (full width at half maximum), given by [4]:

$$F = \pi\sqrt{R} / \left(1 - R\right) \tag{5}$$

It is clear that the finesse F is completely decided by the reflectance R. Thus, for a lossless cavity, for example, we have F = 29.8 for R = 0.9 and F = 312.6 for R = 0.99. Most fiber Fabry-Perot interferometers for sensor applications, however, have low finesses which allow interferometers to operate in a linear region over a larger detection range to the measurand. If $R \ll 1$, the reflectance $R_{\mathrm{F-P}}$ and transmittance $T_{\mathrm{F-P}}$ of fiber Fabry-Perot interferometer can expressed, respectively, as [4]:

$$R_{\mathrm{F-P}} \cong 2R(1 + \cos\phi) \tag{6}$$

$$T_{\mathrm{F-P}} \cong 1 - 2R(1 + \cos\phi) \tag{7}$$

where ϕ is the round-trip propagation phase difference in the interferometer, given by

$$\phi = 4\pi n l_{\mathrm{FP}} / \lambda \tag{8}$$

As sensor applications, the fiber Fabry-Perot interferometer is extremely sensitive to external perturbations that affect the cavity length l_{FP} as well as the refractive index n.

2.5. Fiber Bragg grating-based Fabry-Perot interferometer

As the wavelength selective mirrors, the fiber Bragg gratings also can be used as the intrinsic reflectors in the fiber to construct various types of fiber interferometers, such as the Michelson or Fabry-Perot interferometers.

In the physical structure, as shown in **Figure 2**, a uniform fiber Bragg grating contains a varied refractive index region with a spatial period, distributing along the fiber core within a selected length. A broadband beam propagating in the fiber will interact with each grating plane where only a part of the beam with a specific wavelength matched with the Bragg wavelength of grating will be reflected and propagates in the opposite direction, and the rest of the beam passes through this grating without obvious optical losses [9, 25]. According the mode coupling theory, the Bragg wavelength λ_{B} may be expressed as [11]:

$$\lambda_{\mathrm{B}} = 2n_{\mathrm{eff}}\Lambda \tag{9}$$

where n_{eff} denotes the effective refractive index of the fiber core; Λ is the grating period. From Eq. (9), it is evident that λ_{B} only depends on n_{eff} and Λ. So λ_{B} is very sensitive to ambient temperature and strain imposed on the fiber, which modify n_{eff} and Λ.

http://dx.doi.org/10.5772/66276

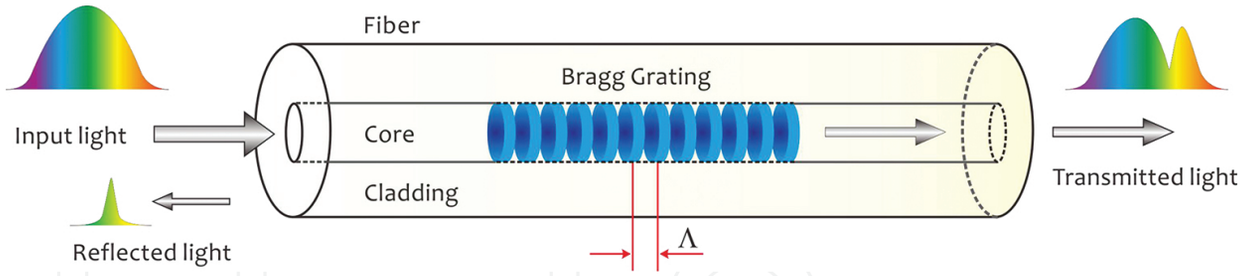

Figure 2. Structure and principle of a fiber Bragg grating.

When two fiber Bragg gratings with identical Bragg wavelengths are imprinted in the same fiber at different positions, as shown in **Figure 1(d)**, a twin-grating-based fiber Fabry-Perot interferometer with an intrinsic cavity is constructed. If a laser beam with wavelength λ is launched into the fiber, when $\lambda = \lambda_B$, two beams partially reflected from both gratings will have a round-trip phase difference $\phi(\lambda)$ as defined in Eq. (8), where l_{FP} is an internal optical path length between two gratings. By assigning the reflectivity and transmission coefficients of each grating as $r_i(\lambda)$ and $t_i(\lambda)$, $i = 1, 2$, respectively, the resultant reflectivity coefficient $r_{FP}(\lambda)$ of twin-grating fiber Fabry-Perot interferometer can be proximately expressed as [26]:

$$r_{FP}(\lambda) \approx r_1(\lambda) + t_1^2(\lambda) r_2(\lambda) e^{-i\phi(\lambda)} \tag{10}$$

When two gratings are of low reflectivity, we have $r(\lambda) = r_1(\lambda) = r_2(\lambda)$, and $t_1(\lambda) = t_2(\lambda) = 1$. So Eq. (10) can be rewritten as

$$r_{FP}(\lambda) \approx r(\lambda)\left[1 + e^{-i\phi(\lambda)}\right] = 2r(\lambda) e^{-i\phi(\lambda)/2} \cos\frac{\phi(\lambda)}{2} \tag{11}$$

The reflectance or power reflectivity $R_{FP}(\lambda) = \left|r_{FP}(\lambda)\right|^2$ of twin-grating fiber Fabry-Perot interferometer is obtained, given by

$$R_{FP}(\lambda) = 2R_B(\lambda) R_m(\lambda) \tag{12}$$

where $R_B(\lambda) = |r(\lambda)|^2$ is the reflectance of single grating, which determines the envelop of the reflection spectrum; $R_m(\lambda) = 1 + \cos(4\pi n l_{FP}/\lambda)$ is the transfer function of the interferometer, which forms the periodically alternating spectral peaks in the reflection spectrum of the interferometer. For an input laser beam with optical power P_0 and wavelength λ_0, the reflected light power from the interferometer will be $P_R = P_0 R_{FP}(\lambda_0)$.

When the interferometer is placed in a varying environment, the reflection spectrum will shift as a whole, as a function of measurand without noticeable changes in its envelop [26]. For a Bragg wavelength shift $\Delta\lambda_B$, which is induced by the measurand, such as temperature or strain, a new reflectance R'_{FP} is obtained as $R'_{FP}(\lambda) = R_{FP}(\lambda - \Delta\lambda_B)$. When the measurand fluctuates, the reflected light power $P_{R'}$ in turn, is altered. This feature has been well utilized in sensor applications for monitoring of the changes in the measurand through the detection of the intensity changes of the interference signal [12].

Figure 3 displays a reflection spectrum of a twin-grating fiber Fabry-Perot interferometer with a 10-mm long intrinsic cavity, measured at 24°C. The Bragg wavelength of each grating is 1542.392 nm and the power reflectivity is about 15%.

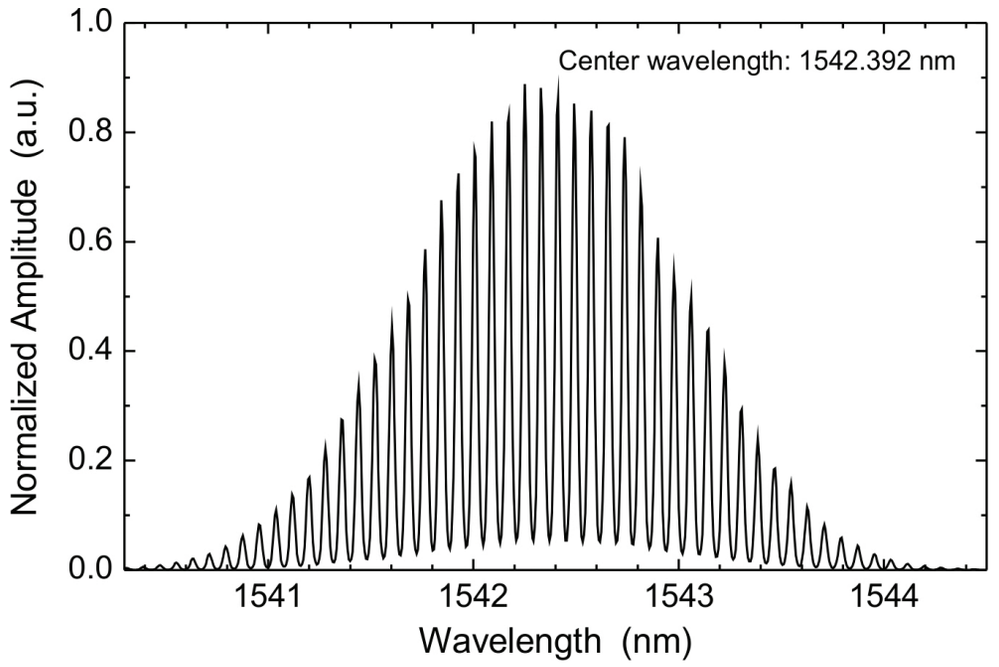

Figure 3. Reflection spectrum of twin-grating fiber Fabry-Perot interferometer.

3. Fiber interferometers for sensor applications

In this section, we will present three selected prototypes of fiber interferometer sensors developed in our laboratory recently, which are intentionally employed in the electric power industry for partial discharge sensing as well as for power-frequency electric field measurements. Some preliminary experimental results for demonstrating the performances of these sensors and experimental systems also are presented. The prototypes to be presented below will include: a fiber Sagnac interferometer-based acoustic sensor, a fiber Fabry-Perot interferometer-based acoustic sensor, and a twin-grating fiber Fabry-Perot interferometer-based power-frequency electric field sensor.

http://dx.doi.org/10.5772/66276

3.1. A fiber Sagnac interferometer-based acoustic sensor

In the previous work, we had proposed a novel fiber Sagnac interferometer-based acoustic sensor for sensing of high-frequency and weak ultrasonic waves produced by the partial discharges [18].

3.1.1. System configuration and operation principles

The scheme of the proposed sensor is presented in **Figure 4(a)**, which is based on a fiber Sagnac interferometer consisting of a 3-dB, 2 × 2 fiber coupler (OC) and two no-isolator, CW DFB lasers (LD_1 and LD_2) with two nearly identical lasing wavelengths at 1528.60 nm and 1529.38 nm, respectively. Two AC current signals i_1 and i_2 are obtained, respectively, from the corresponding photodiodes packaged in laser modules. The final detection signal i_3 is constructed through a cross-correlation operation with i_1 and i_2. A fiber polarization controller PC in the fiber loop is utilized to adjust the total birefringence of the fiber. The fiber loop made of a 1-km long single-mode fiber forms a sensor coil with a diameter of 60 mm. The outer layers of this coil, close to one end of the OC, are utilized as the sensing region, so that the relatively high sensitivity can be achieved.

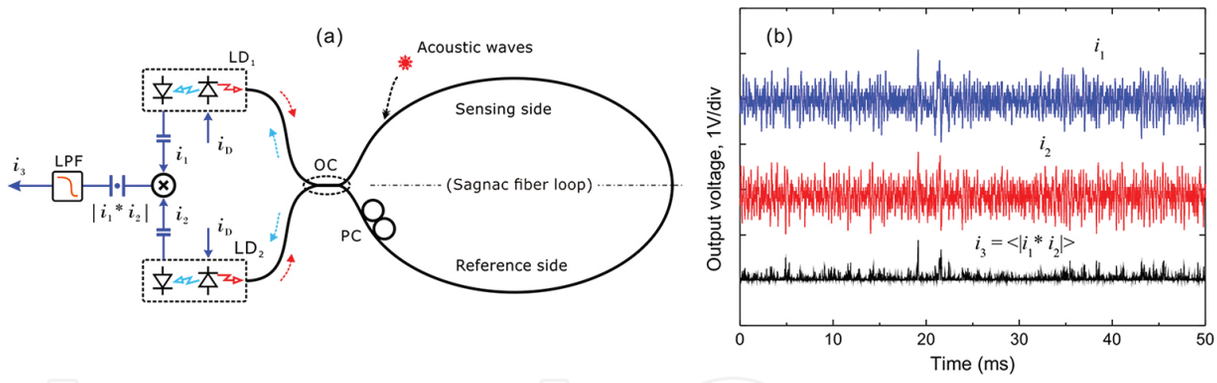

Figure 4. (a) Scheme of proposed fiber acoustic sensor and (b) a group of output waveforms obtained in a static state.

The feature of this sensor is to employ two laser diodes without optical isolators as two individual light sources to illuminate the fiber Sagnac interferometer from two sides, and at the same time, also as two in-line optical amplifiers to enhance the intensities of signal beams from the Sagnac interferometer. So the sensitivity of this sensor, compared with other sensors with the normal configuration, has a significant enhancement.

In principle, this sensor is a balanced fiber Sagnac interferometer, which, in the structural analysis, can be regarded as two individual Sagnac interferometers with a mirror-image relation. According to the analysis methods proposed in Ref. [19], for a balanced fiber Sagnac interferometer, two fringe signals i_1 and i_2 including laser intensity noises can be expressed as

$$i_1 \propto -I_0 \sin\phi_b \sin\Delta\varphi + n_{LD_1} \tag{13}$$

$$i_2 \propto +I_0 \sin\phi_b \sin\ \Delta\varphi + n_{LD_2} \tag{14}$$

where I_0 is the average intensity of laser beams; ϕ_b is the nonreciprocal phase difference between two beams propagating in the fiber coil, which is a constant and arises from the fiber birefringence; $\Delta\varphi$ is another phase difference between two beams, caused by external disturbances; n_{LD_1} and n_{LD_2} are the intensity noises in two laser diodes, which all can be regarded as a zero-mean, additive white Gaussian noise process.

After taking a cross-correlation operation by simply multiplying i_1 and i_2, the final detection signal i_3 is obtained, expressed as

$$i_3 = \langle |i_1 \cdot i_2| \rangle \propto I_0^2 \sin\phi_b{}^2 \sin\Delta\varphi^2 \tag{15}$$

where $|\cdot|$ represents an absolute value operation; $\langle \cdot \rangle$ denotes a time average realized in electric circuit by a low-pass filter (LPF), and all intensity noise items included in i_1 and i_2 will be removed after this time-average operation. The item $\sin\phi_b$ above is defined as the fringe visibility or the scale factor [19], which can be maximized by adjusting the PC to achieve $\phi_b = \pi/2$.

3.1.2. Experimental results

We carried out several experiments based on this proposed sensor system. **Figure 4(b)** shows a group of signal waveforms obtained in a static state. The amplitude fluctuations in i_1 and i_2 traces reflect the intensity noises in laser beams. However, in i_3 trace, these intensity noises have been obviously suppressed. As a direct benefit, the signal-to-noise ratio (SNR) of this sensor system is significantly improved.

We attempted to detect the acoustic emissions generated by high-voltage discharges between two electrodes. An experimental setup is illustrated in **Figure 5**, in which a pair of pin-type electrodes, connected with an AC high-voltage generator, was placed in an oil tank which was filled with transformer oil. The electrode gap was set at 8 mm. The fiber coil was attached to the shell of the oil tank, facing the electrodes. **Figure 6(a)** shows two groups of acoustic wave signals recorded at two time periods separated by about 10 seconds, when the imposed AC voltage was increased close to 5 kV and the discharges just started. It is obvious that, as shown in two signal traces, in this stage, the discharges in oil present a periodical change in intensity with a 50-Hz repetition frequency and the average intensity increases with time. **Figure 6(b)** displays a signal trace recorded a minute later. In this stage, the oil had become hot and dirty

due to the discharge arcs burning the oil. Clearly, in this result, the signal amplitudes increase greatly and the repetition frequency of discharges then changes to 100 Hz, which indicates that the oil will be in a complete breakdown state and an oil-burning will come soon.

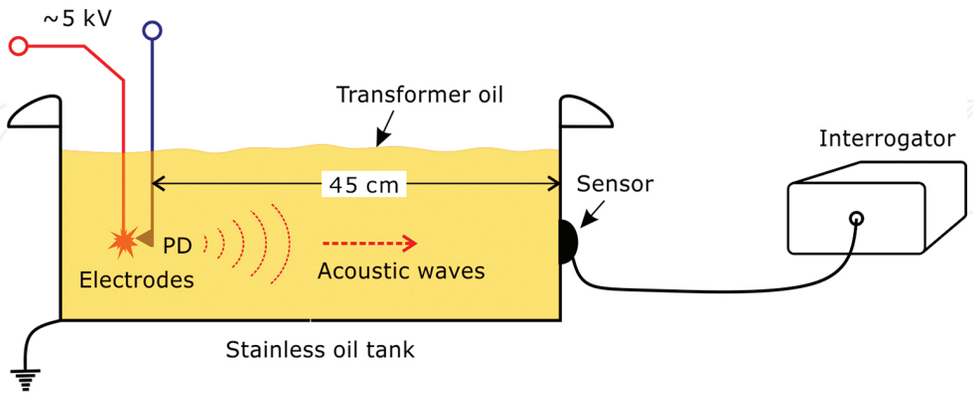

Figure 5. Schematic of an experimental setup for sensing of partial discharges in oil tank.

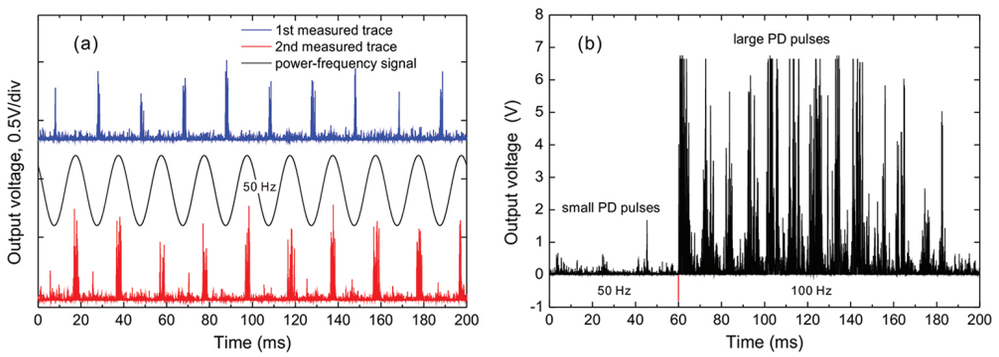

Figure 6. Measured partial discharges occurred in transformer oil. (a) A group of signal waveforms measured when partial discharges just started, and (b) signal waveforms measured a minute later.

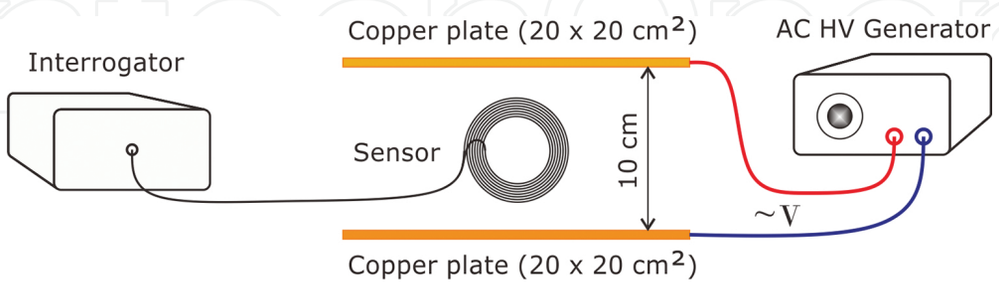

Figure 7. Schematic of an experimental setup for electric field strength measurements.

We also tried to employ this sensor system to measure the strength of power-frequency electric field by detecting of the intensities of ultrasonic waves propagated in air, which were produced between two electrodes during ionization of air by the AC high-voltage electric field. The

experimental setup is illustrated in **Figure 7**, in which the fiber coil was placed between two parallel, copper-plate electrodes separated by 10 cm.

In the experiment, the AC voltage imposed on the electrodes was increased gradually and the detection signals were recorded at several specified voltages. **Figure 8(a)** shows three groups of pulse train waveforms, recorded at 1800 V, 2800 V, and 3800 V, respectively. By observing these data, it is obvious that the number of pulses or pulse density within a cycle of AC voltage increases with the imposed AC voltage.

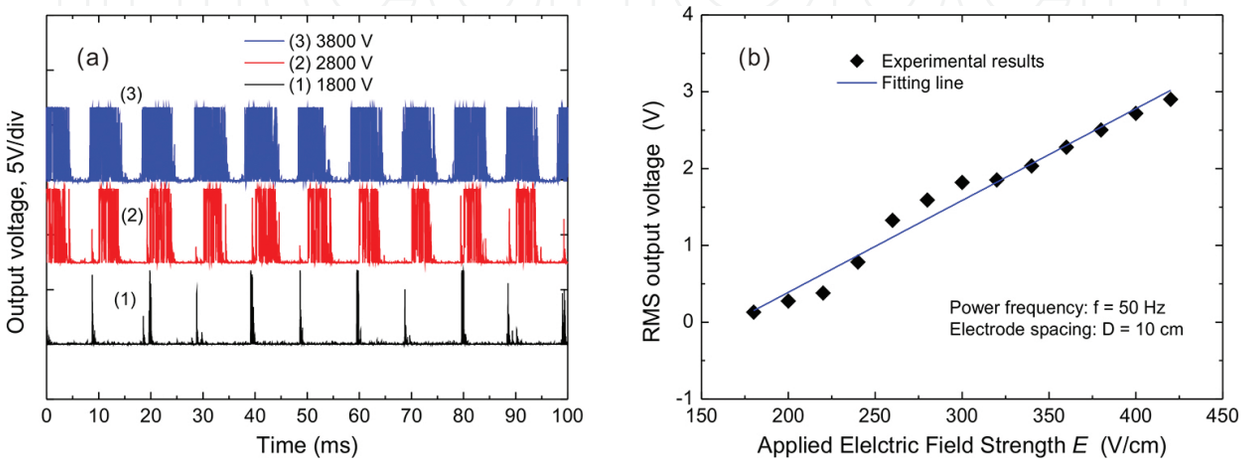

Figure 8. (a) Measured ultrasonic waves generated by air ionization, and (b) relationship between RMS output voltage and applied electric field strength.

Figure 8(b) shows a set of RMS (root-mean-square) voltages measured in a cycle of AC voltage under different electric field strengths from 175 to 475 V/cm. It is obvious that the RMS voltage increases proportionally with the applied electric field strength.

3.2. A fiber Fabry-Perot interferometer-based acoustic sensor

Another novel acoustic sensor based on the fiber Fabry-Perot interferometer is demonstrated. This sensor is specifically designed to be workable in the transformer oil to monitor the partial discharges occurred inside the power transformer.

3.2.1. System configuration and operation principles

The scheme of the proposed sensor system is presented in **Figure 9**, in which a CW DFB laser diode without the optical isolator was employed as the light source, as well as an in-line optical amplifier. The detection signals are obtained from a photodetector packed in laser module. A ferrule-type sensor head is constituted by inserting a single-mode fiber with a flat-cut end into a ceramic ferrule and leaving a 1-mm long space for forming an extrinsic cavity, as shown in **Figure 9**. When the sensor head is immersed into the transformer oil, the oil will permeate into the ceramic ferrule and stop before the fiber end, which forms an extrinsic cavity with two low-reflectance reflectors, the fiber end and the oil surface. The refractive index of transformer oil is estimated in the range 1.40–1.48, close to that of the fiber core, varying with the oil type

http://dx.doi.org/10.5772/66276

and quality as well as with the oil temperature. According to the analyses in Section 2.4, the output current signal I_{out} can be expressed as

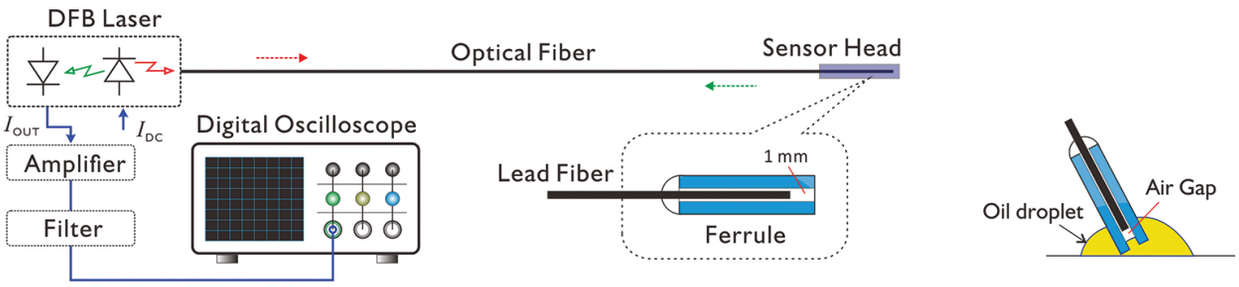

Figure 9. Schematic of a fiber Fabry-Perot interferometer-based acoustic sensor and structure of sensor head.

$$I_{out} \propto 2GP_0R\left(1+\cos\phi\right) \tag{16}$$

where G is the gain of laser diode when it is taken as an in-line optical amplifier; P_0 is the optical power launched into the sensor; R is an average reflectance of two reflectors; $\phi = 4\pi l_{FP}/\lambda$ is the round-trip phase difference; and l_{FP} denotes the cavity length. When the partial discharges arise inside the power transformer, ultrasonic waves induced by discharges will propagate in the transformer oil in all directions. The energy of these induced ultrasonic waves mainly distributes in a frequency range of 50–150 kHz [14]. When some of ultrasonic waves arrive at the sensor, the acoustic pressures will modulate the phase difference ϕ by changing the oil level inside the ferrule, in turn, the cavity length l_{FP}, which, as a result, causes the signal I_{out} to change its amplitude. So that by detecting I_{out}, the partial discharges occurred in the power transformer can be monitored.

3.2.2. Experimental results

Figure 10 shows a set of the spectra of the sensor, measured when the sensor was placed in the air as well as was immersed into the transformer oil at different depths (>10 cm). From these results, clearly, the spectrum of the sensor at each depth is of a periodical change characteristic, and the spectral interval between adjacent dips becomes wider as the increase of immersion depth. It indicates the fact that the oil entering into the ceramic ferrule and the fiber end virtually had formed an extrinsic cavity of the fiber Fabry-Perot interferometer.

We experimentally investigated the sensor sensitivity with a setup shown in **Figure 11**, in which the sensor head was placed on a Bakelite plate table and inserted into a silicon oil droplet, here as acoustic wave couplant and also as optical reflection medium. In the experiment, a tiny, 2-cm long metal pin freely falling down from 2-cm height hit the table to generate the weak Lamb waves which propagated in the Bakelite plate and finally arrived at the sensor head in a 45-cm distance. A series of wave signals detected by our sensor is

clearly shown in **Figure 12**, which demonstrates that the proposed sensor has a very high sensitivity in detection of weak Lamb waves propagating in the Bakelite plate.

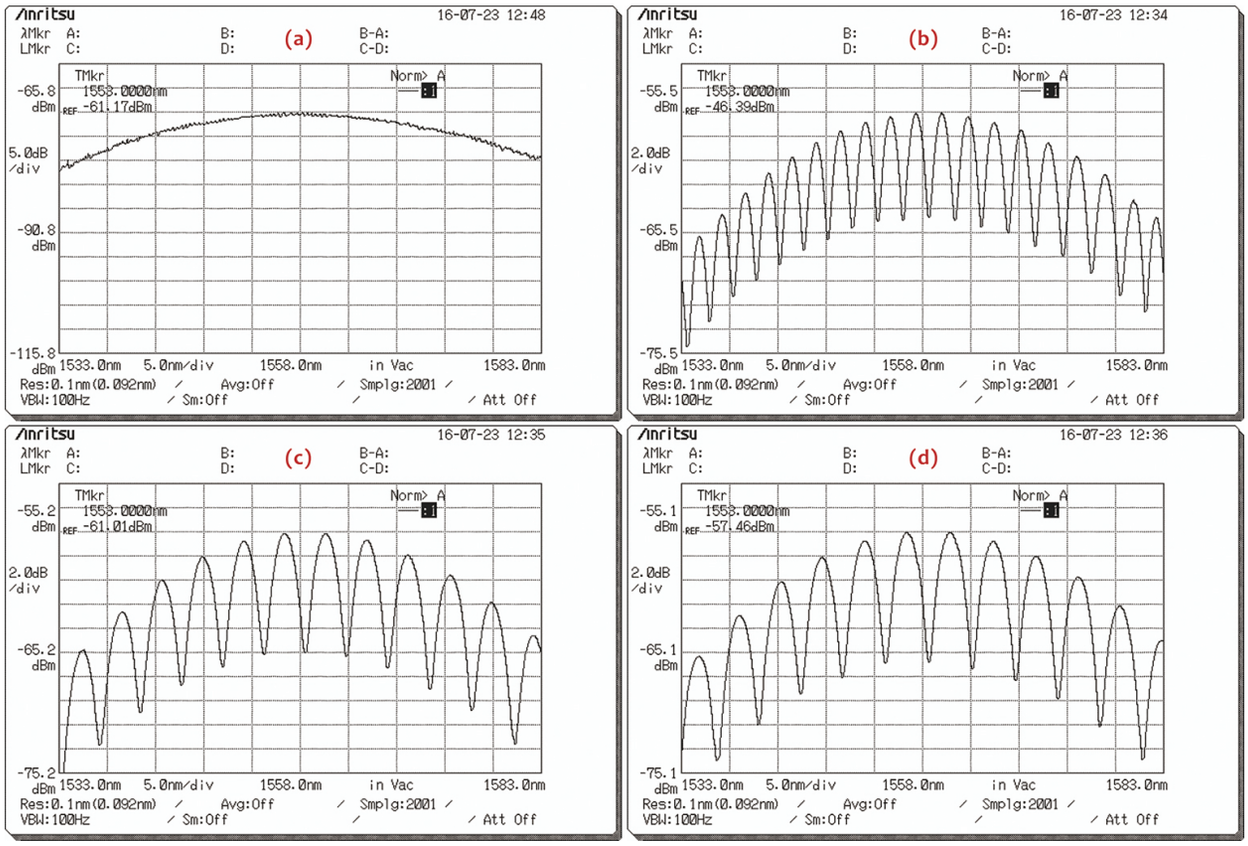

Figure 10. Sensor output spectra measured in air (a) and in transformer oil (b–d) at different depths.

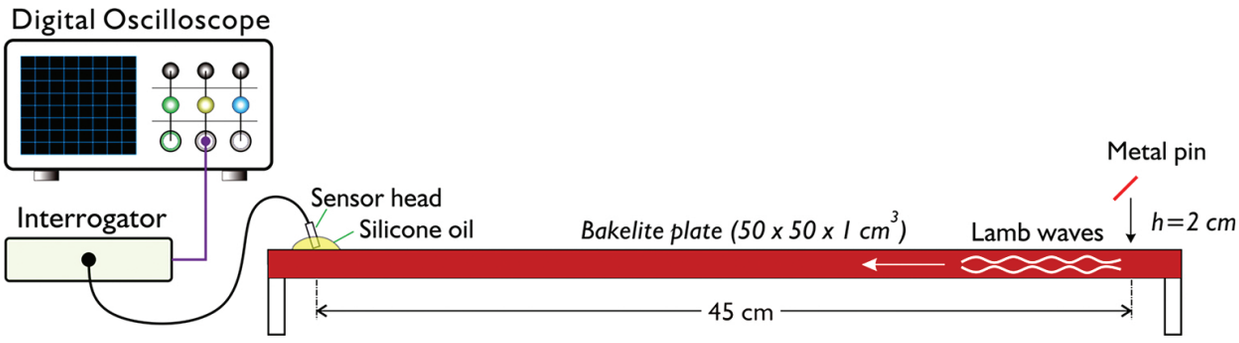

Figure 11. Schematic of an experimental setup for evaluating of sensor sensitivity.

An experiment was carried out for testing the sensor performances in detections of the partial discharges occurred in the transformer oil. **Figure 13** shows a set of photos on this experimental setup. One shown in **Figure 13(a)** is a photo of the hand-made sensor prototype. As shown in **Figure 13(b)**, the sensor was inserted into an 850-mm long PVC pipe filled with transformer

http://dx.doi.org/10.5772/66276

oil and a pair of pin-type electrodes was inserted into the other end of the pipe. In the experiment, the AC voltage imposed on the electrodes was increased gradually until the discharges arose. During this process, the sensor outputs were monitored and recorded.

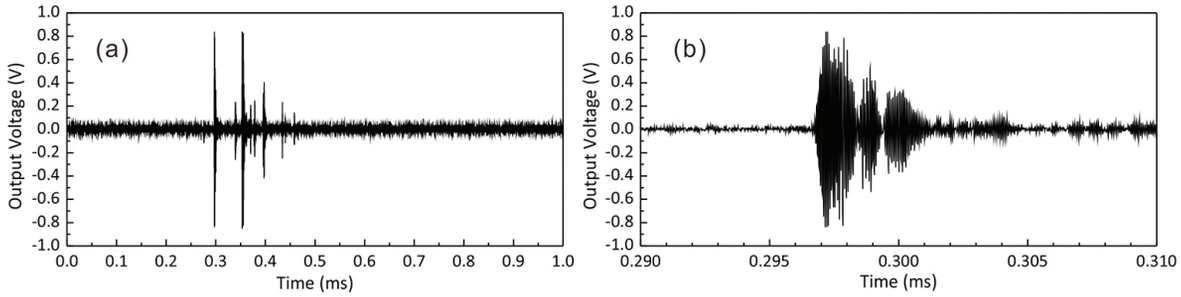

Figure 12. (a) Measured Lamb wave signals and (b) waveforms around 0.3 ms.

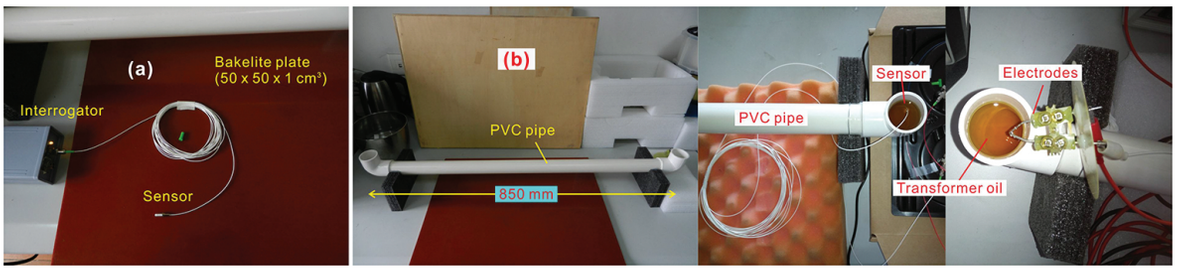

Figure 13. A group of photos on (a) sensor prototype and (b) experimental setup and relevant parts.

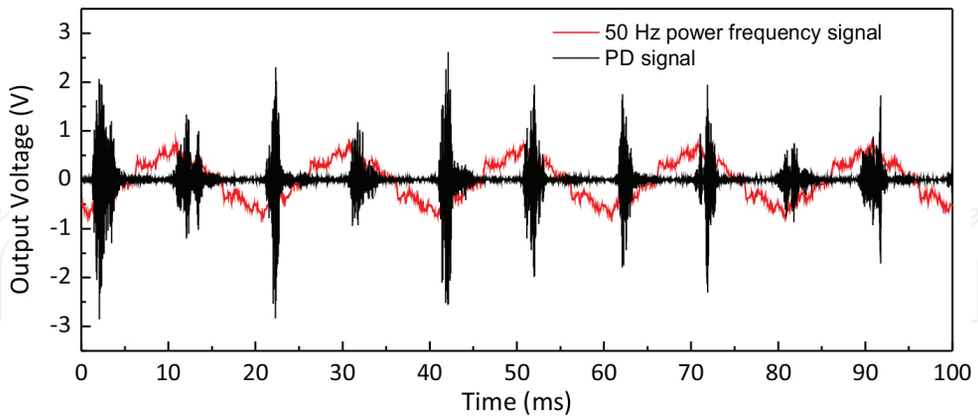

Figure 14. Measured partial discharge signals in transformer oil.

Figure 14 shows a set of measured signal waveforms. The red-line trace is a power-frequency signal measured as a phase reference here, and the black-line trace is the acoustic signals measured when the discharges arose in the transformer oil. From these data, clearly, the proposed sensor can work in the transformer oil to directly detect the internal ultrasonic waves induced by discharges.

Compared with other sensors proposed in [20, 21] with similar structures, this sensor does not need the diaphragm as a reflector, which resultantly make it simpler in fabrication and more sensitive to ultrasonic waves propagating in the transformer oil.

3.3. A twin-grating fiber Fabry-Perot interferometer-based power-frequency electric field sensor

We will demonstrate an all-fiber power-frequency electric field sensor, based on a twin-grating fiber Fabry-Perot interferometer. This sensor technology intentionally is applied in the power industry for measuring of the power-frequency electric field strength near the high-voltage equipment.

Compared with other types of optical electric field sensing technologies based on several physical effects, such as Pockels, Kerr, piezoelectric, or electrostrictive effect [27–30], our electric filed sensing technology is based on the electrical polarization properties [28, 31] of the dielectric coating material with a variety of attractive features, such as small size, low cost, electrodeless, single-lead, high sensitivity, flexibility in a variety of environments and capability of remote sensing.

3.3.1. System configuration and operation principles

As schematically illustrated in **Figure 15(a)**, this fiber electric field sensor actually is a twin-grating fiber Fabry-Perot interferometer-based vibration sensor [32]. In this sensor structure, a polyimide-coated, single-mode fiber including two identical gratings is clamped at a position close to the first grating by a fiber holder to form a fiber vibration sensor with the cantilever beam structure [33, 34]. The length of cantilever beam is chosen so that the cantilever beam has a natural frequency close to the power frequency of 50 Hz or 60 Hz. The polyimide coating adopted in this structure is first to protect the fiber gratings as well as to enhance the mechanical strength of fiber cantilever beam, and second to get an excitation power for vibration (see **Figure 15(b)**) from the applied alternating electric filed by means of the electrical polarization properties of polyimide film.

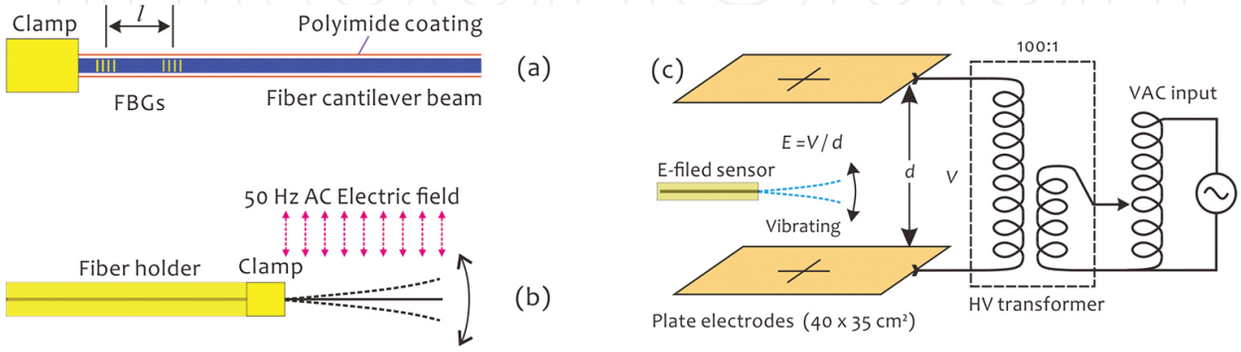

Figure 15. Schematics of electric field sensor structure (a), principle (b), and test setup (c).

http://dx.doi.org/10.5772/66276

The polyimide-coated fiber actually holds a trace of charged ions stored among polyimide crystalline layers, which make this fiber appear to have weak electrical polarization properties [31, 35]. As we assume, the charged ions may originate from the electrification occurred in the coating process, when the fiber was repeatedly painted with a brush filling with polyimide resin, or come from the electrostatic charging [36–38] under a high potential field environment. According to our observations and tests, the polyimide favors to trap the negative ions, so it is the polar dielectric [31], showing the electronegative characteristic. Since the polyimide is a dielectric with a relative permittivity $\varepsilon_r = 3.4$ at a frequency of 1 kHz at room temperature, and also as one kind of high-quality electrical insulation material, widely used in the power industry, some of the trapped net negative ions probably can be stored permanently or semi-permanently in polyimide crystalline layers after the polyimide resin is heat-cured.

When a fiber with polyimide coating in a loose state is placed into a power-frequency electric field, it starts to jitter under the action of alternating electric field force. However, this jittering is very small in amplitude and irregular, which can not bring us any useful information about surrounding electric field strength. A cantilever beam structure, as employed in many types of vibration sensors [32], can be utilized, in this case, to regularize the fiber's jittering and convert it into a regular mechanical vibration. Furthermore, the vibrating amplitude can be mechanically amplified over hundred times by adjusting the natural frequency of the cantilever beam and bringing it close to the power frequency.

Since the vibrating amplitude of the cantilever beam is proportional to the induced electric field force, in turn, the electric field strength, it is possible to evaluate the electric field strength by means of interferometric methods to measure the vibrating amplitude of cantilever beam. This can be realized with our sensor system to be introduced next by detecting the fringe signal intensity proportional to the vibrating amplitude of cantilever beam.

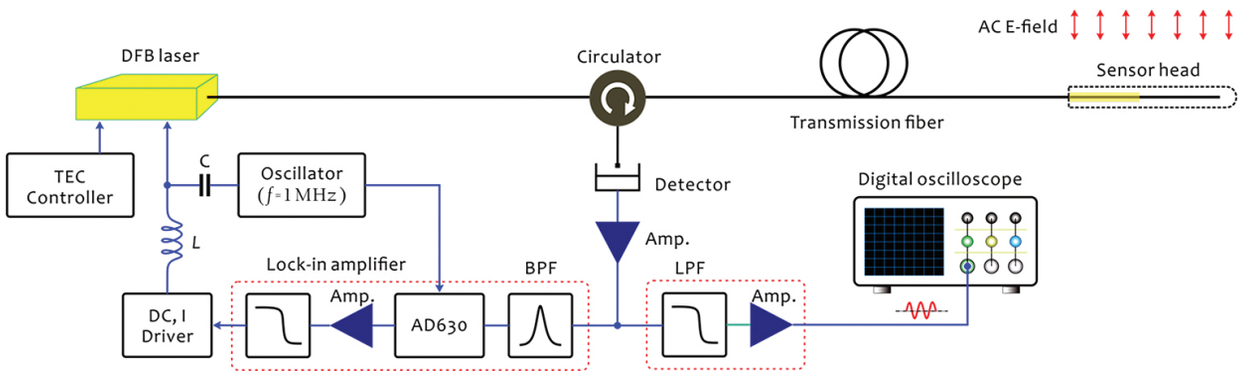

Figure 16. Schematic of electric field sensor system configuration.

The configuration of a sensor system is schematically shown in **Figure 16**, which consists of a CW DFB laser diode, an optical circulator, and a photodetector. The reflection spectrum of sensor is shown in **Figure 3**. The sensor operation is maintained at a quadrature point of the fringe signal by adjusting the laser wavelength with a feedback arrangement to get a quasi-linear dependence of reflected light power on the phase shift produced by vibration. The

detected electrical signals after passing a low-pass filter are sent into a digital oscilloscope for waveform display and signal processing. An experimental setup for evaluating sensor performances is shown in **Figure 15(c)**. In the experiments, the sensor was placed between two parallel electrodes which generated a uniform electric field in this space.

In operating principle, when the sensor vibrates under the action of alternating electric field force, the Bragg wavelength of twin-grating-based fiber Fabry-Perot interferometer will be modulated by varying axial strains in the fiber, created by periodic bending of fibers, proportional to the vibrating amplitude, which in turn changes the reflected light power and generates a sinusoid fringe signal with an average amplitude proportional to the electric field strength.

3.3.2. Experimental results

A set of photos showing sensor prototype, experimental setup and sensor vibrating under the action of alternating electric field force is shown in **Figure 17**. The sensor shown in **Figure 17(a)** has a 40-mm long cantilever beam with a natural frequency at 50 Hz. The beam length depends on the power frequency and the hardness of coating material, varying from 39 to 40 mm. The frequency responses of the sensor can be investigated with a frequency-swept shaker. A photo in **Figure 17(a)** shows the sensor vibrating under a 50-Hz, 5-kV electric field environment **Figure 17(b)** is a photo of the experimental setup.

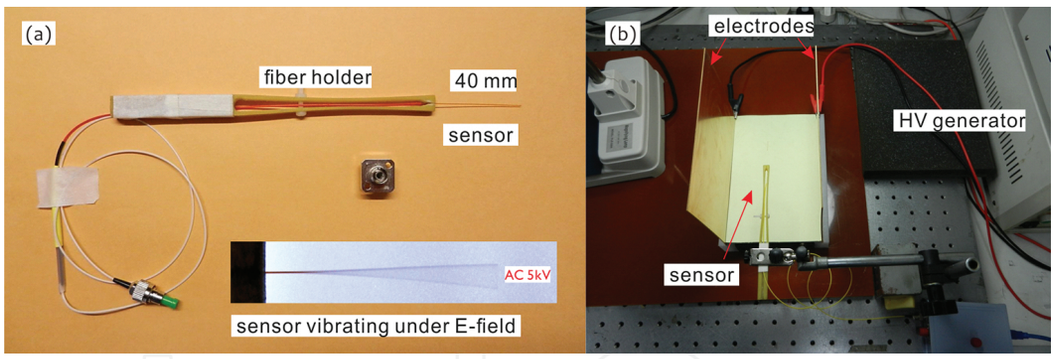

Figure 17. A set of photos on sensor (a) and experimental setup (b).

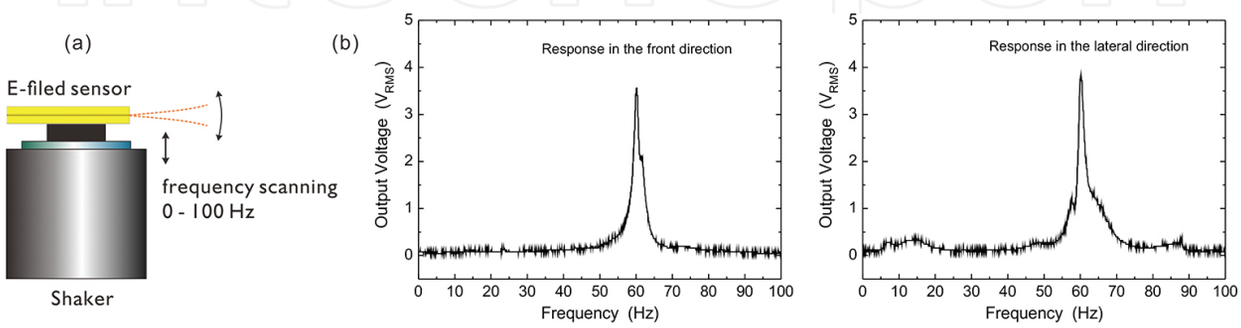

Figure 18. Test for investigating frequency response of sensor with a shaker (a) and results (b).

Figure 18(b) shows two test results on the frequency response distributions of the sensor in two orthogonal directions, the front direction and lateral direction, obtained with a frequency-swept shaker as schematically shown in **Figure 18(a)**. This experiment was to investigate the natural frequency of the sensor, which was designed initially at 60 Hz. The beam length in this case was 39.2 mm. From the test results, clearly, this sensor only has a natural frequency at 60 Hz in both orthogonal directions in the frequency range of 0–100 Hz.

With the experimental setup shown in **Figure 15(c)** as well as in **Figure 17(b)**, we carried out several experiments for investigating sensor performances as well as for verifying the feasibility of the proposed sensor with respect to electric field sensing.

Figure 19(a) shows a measured electric field signal (inset graph) and its frequency distribution from 0 to 100 Hz. In this measurement, the sensor was placed between two electrodes separated by 10 cm, which were connected to 60-Hz, 3000-V voltage. **Figure 19(b)** shows a group of measured RMS voltages of signal amplitude under different AC voltages, varying from 0 to 5 kV. The test arrangement is schematically delineated in **Figure 19(b)**. From these results above, clearly, the 60-Hz sinusoid wave, as a typical vibration signal, really reflects a power-frequency electric field force acting on the sensor, and the RMS voltage of signal amplitude is proportional to the applied electric field strength in a relation $E = \mathrm{V}/\mathrm{D}$.

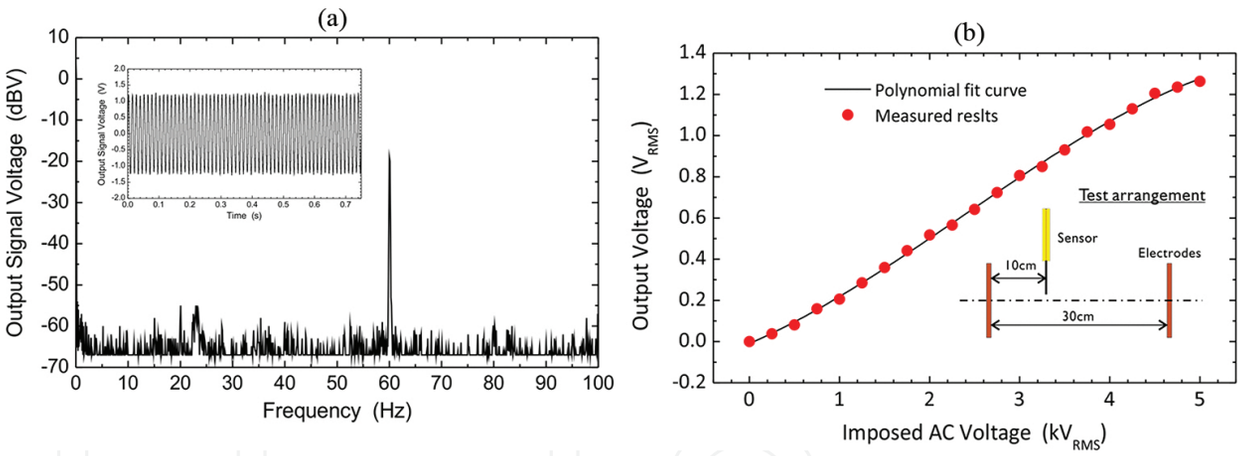

Figure 19. (a) Measured electric field signal waveform at 60-Hz power frequency (inset graph) and its FFT, and (b) relationship between measured RMS voltage and imposed AC voltage.

4. Conclusion

In this chapter, basic concepts of optic interferometry have been presented and clarified. Four main types of fiber interferometers with the help of simple mathematical descriptions also have been briefly introduced. By means of the wavelength of the light source as the length unit as well as the period of light wave as the time unit, optical interferometry is a precision metrology. Combined with the merits of optical interferometry and optical fiber, fiber-optic interferometers have many unique features capable of satisfying a variety of

needs in industrial measurement fields, and can provide a much higher sensitivity than their bulk-optic versions, since the optical fiber can be rolled to form a coil which extremely extends the optical path in a limited space. The main applications of fiber-optic interferometers now are in sensor fields as fiber-optic sensors to detect various physical parameters with high accuracy and sensitivity.

Many properties of optical fiber, such as the random birefringence distributions along the fiber, temperature dependency, dispersion, and nonlinearity, however, sometimes become main factors to influence the ultimate performances of a fiber interferometer sensor. Therefore, when we design a fiber interferometer sensor or explore its new applications, these factors should be taken into account. Due to a limit of the number of pages, these properties of the optical fiber as well as their impact on sensor performances, however, have not been mentioned yet in this chapter.

Three novel fiber-optic sensor models, based on optical interferometry technologies and developed in our laboratory recently, have been proposed and demonstrated. Experimental results mainly used for describing basic sensing concepts and sensor structures, as well as for demonstrating sensor performances also were presented, although these are not all of our research achievements. These fiber interferometer sensors are intentionally used, in the future, in the electric power industry as one of most important application fields of fiber-optic interferometer sensing technologies, for various physical parameter measurements, which may be difficult for electric/electronic sensors.

Many research activities are in progress to characterize these proposed fiber sensors in respect of the sensitivity, directionality, frequency responses, and stability. Also how to pack these fiber sensors to make them useful in practical applications is still a challenging work.

Acknowledgements

This work is supported by the National Natural Science Foundations of China (Grant No. 61377082).

Author details

Lutang Wang* and Nian Fang

*Address all correspondence to: ltwang@mail.shu.edu.cn

Key Laboratory of Specialty Fiber Optics and Optical Access Networks, School of Communication and Information Engineering, Shanghai University, Shanghai, China

References

[1] Langenbeck, P., editor. Interferometry for precision measurement. Bellingham, Washington USA: SPIE; 2014. 244 p. DOI: 98227–0010.

[2] Hariharan, P., editor. Basics of interferometry. 2nd ed. Boston: Academic Press; 2007. 213 p.

[3] Culshaw, B. Fiber optics in sensing and measurement. IEEE Journal of Selected Topics in Quantum Electronics 2000; 6: 1014–1021.

[4] Udd, E., editor. Fiber optic sensors: An introduction for engineers and scientists. Hoboken, New Jersey, USA: John Wiley & Sons, Inc.; 2006. 467 p.

[5] Berthold III, J.W. Industrial applications of fiber optic sensors. In Fiber optic sensors: An introduction for engineers and scientists; Udd, E.; New Jersey USA: John Wiley & Sons, Inc.; 1991, 2006; pp. 409–437.

[6] Udd, E. Fiber-optic acoustic sensor based on the Sagnac interferometer. In Single Mode Optical Fibers 90, Proc. of SPIE 1983; 0425: 90–95.

[7] Rajkumar, N.; Jagadeesh Kumar, V.; Sankaran, P. Fiber sensor for simultaneous measurement of current and voltage in a high-voltage system. Applied Optics. 2005; 32(7): 1125–1128.

[8] Lopez-Higuera, J.M., editor. Handbook of optical fiber sensing technology. Chichester, England: John Wiley & Sons Ltd.; 2002. 789 p.

[9] Mihailov, S.J. Fiber Bragg grating sensors for harsh environments. Sensors. 2012; 12: 1898–1918. DOI: 10.3390/s120201898

[10] Blackburn, T.R.; Phung, B.T.; James, R.E. Optical fibre sensor for partial discharge detection and location in high-voltage power transformer. In Sixth International Conference on Dielectric Materials, Measurements and Applications 1992; 33–36.

[11] Kersey, A.D.; Davis, A.M.; Patrick, J.H.; LeBlanc, M.; Koo, K.P.; Askins, C.G.; et al. Fiber grating sensors. Journal of Lightwave Technology. 1997; 15(8): 1442–1463.

[12] He, X.; Taylor, H.F. Intrinsic fiber Fabry-Perot temperature sensor with fiber Bragg grating mirrors. Optics Letters. 2002; 27(16): 1388–1390.

[13] Rashleigh, S.C. Origins and control of polarization effects in single-mode fibers. Journal of Lightwave Technology. 1983; LT-1: 312–331.

[14] Posada, J.E.; Rubio-Serrano, J.; Garcia-Souto, J. A. All-fiber interferometric sensor of 150 kHz acoustic emission for the detection of partial discharges within power transformers. In 21st International Conference on Optical Fiber Sensors, Proc. of SPIE 2011; 7753: 77531S:1–77531S:4.

[15] Harvey, D.; McBride, R.; Barton, J.S.; Jones, J.D.C. A velocimeter based on the fiber optic Sagnac interferometer. Measurement Science and Technology. 1992; 3: 1077–1083.

[16] Burns, W.K.; Chen, C.L; Moeller, R.P. Fiber-optic gyroscopes with broad-band sources. Journal of Lightwave Technology. 1983; LT-1: 98–105.

[17] Carolan, T.A.; Reuben, R.L.; Barton, J.S.; Jones, J.D.C. Fiber-optic Sagnac interferometer for noncontact structural monitoring in power plant applications. Applied Optics. 1997; 36: 1504–385.

[18] Wang, L.T.; Fang, N.; Huang, Z.M. A novel Sagnac-based fiber-optic acoustic sensor using two laser diodes with external optical injections. In: Kennis Chen, editor. Testing and Measurement: Techniques and Applications; 16–17 Jan. 2015; Phuket Island, Thailand. London: CRC Press/Balkema; 2015. pp. 145–150.

[19] Wang, L.T.; Fang, N.; Wu, C.; Qin, H.; Huang, Z. A fiber optic PD sensor using a balanced Sagnac interferometer and an EDFA-based DOP tunable fiber ring laser. Sensors. 2014; 14(5): 8398–8422. DOI: 10.3390/s140508398

[20] Chin, K.K.; Sun, Y.; Feng, G.; Georgiou, G.E.; Guo, K.; Niver, E. et al. Fabry Perot diaphragm fiber-optic sensor. Applied Optics. 2007; 46: 7614–7619.

[21] Cibula, E.; Donlagic, D. Miniature fiber-optic pressure sensor with a polymer diaphragm. Applied Optics. 2005; 44(10): 2736–2744.

[22] Satoshi, A.; Tanaka, S.; Takahashi, N. High-sensitivity vibration sensing using in-fiber Fabry-Perot interferometer with fiber-Bragg-grating reflectors. In 20th International Conference on Optical Fibre Sensors, Proc. of SPIE 2009; 7503: 75033L:1–75033L:4.

[23] Xie, Z. Two applications of the Fabry-Perot interferometric sensor. Ph.D. Thesis, Texas A&M University: College Station, TX, USA, August 2006.

[24] Dong, B.; Han, M.; Wang, A. Two-wavelength quadrature multipoint detection of partial discharge in power transformers using fiber Fabry-Perot acoustic sensors. In Fiber Optic Sensors and Applications IX, Proc. of SPIE 2012; 8370: 83700K:1–83700K:11.

[25] Majumder, M.; Gangopadhyay, T.K.; Chakraborty, A.K.; Dasgupta, K.; Bhattacharya, D.K. Fiber Bragg gratings in structural health monitoring–present status and applications. Sensors and Actuators A. 2008; 147:150–164.

[26] Miridonov, S.V.; Shlyagin, M.G.; Tentori, D. Twin-grating fiber optic sensor demodulation. Optics Communications. 2001; 191(2001): 253–262.

[27] Bohnert, K.M.; Nehring, J. Fiber-optic sensing of electric field components. Applied Optics. 1988; 27(23): 4814–4818.

[28] Zahn, M. Optical, electrical and electromechanical measurement methodologies of field, charge and polarization in dielectrics. IEEE Transactions on Dielectrics and Electrical Insulation. 1998; 5(5): 627–650.

[29] Koo, K.P.; Sigel, G.H. An electric field sensor utilizing a piezoelectric Polyvinylidene Fluoride (PVF2) film in a single-mode fiber interferometer. IEEE Journal of Quantum Electronics. 1982; QE-18(4): 670–675.

[30] Tomic, M.C.; Elaza, J.M. Voltage measurement based on the electrostrictive effect with simultaneous temperature measurement using a 3 × 3 fiber-optic coupler and low coherence interferometric interrogation. Sensors and Actuators A. 2004; 115: 462–469.

[31] Raju, G.G., editor. Dielectrics in electric fields. New York, NY USA: Marcel Dekker, Inc.; 2003. 570 p.

[32] Zhu, Y.; Shum, P.; Lu, C.; Lacquet, B.M.; Swart, P.L.; Spammer, S. J. Temperature-insensitive fiber Bragg grating accelerometer. IEEE Photonics Technology Letters. 2003; 15(10): 1437–1439.

[33] Todd, M.D.; Johnson, G.A.; Althouse, B.A.; Vohra, S. T. Flexural beam-based fiber Bragg grating accelerometers. IEEE Photonics Technology Letters. 1998; 10(11): 1605–1607.

[34] Leissa, A.W.; Sonalla, M.I. Vibrations of cantilever beams with various initial conditions. Journal of Sound and Vibration. 1991; 150(1): 83–99.

[35] Gerhard, R. A matter of attraction: electric charges localised on dielectric polymers enable electromechanical transduction. In: 2014 Annual Report Conference on Electrical Insulation and Dielectric Phenomena; IEEE; 2014. pp. 1–10.

[36] Watson, P.K. The transport and trapping of electrons in polymers. IEEE Transactions on Dielectrics and Electrical Insulation. 1995; 2(5): 915–924.

[37] Albrecht, V.; Janke, A.; Nemeth, E.; Spange, S.; Schubert, G.; Simon, F. Some aspects of the polymers' electrostatic charging effects. Journal of Electrostatics. 2009; 67: 7–11.

[38] Bartnikas, R. Performance characteristics of dielectrics in the presence of space charge. IEEE Transactions on Dielectrics and Electrical Insulation. 1997; 4(5): 544–557.

IntechOpen